International Journal of Mechanical Sciences 238 (2023) 107829

Contents lists available at ScienceDirect

International Journal of Mechanical Sciences

journal homepage: www.elsevier.com/locate/ijmecsci

Acoustic metamaterials with controllable bandgap gates based on magnetorheological elastomers

Vyacheslav N. Gorshkov [a,b], Oleksii V. Bereznykov [a], Gernot K. Boiger [c], Pooya Sareh [d], Arash S. Fallah [e,f,*]

[a] Igor Sikorsky Kyiv Polytechnic Institute, National Technical University of Ukraine, 37 Prospect Peremogy, Kiev 03056, Ukraine
[b] Department of Chemistry and Biomolecular Science, Clarkson University, Potsdam, NY 13699, USA
[c] Institute of Computational Physics, Zürich University of Applied Sciences, Wildbachstrasse 21, Winterthur 8400, Switzerland
[d] Department of Mechanical and Aerospace Engineering, Creative Design Engineering Lab (Cdel), School of Engineering, University of Liverpool, Liverpool L69 3GH, UK
[e] Department of Mechanical, Electronic and Chemical Engineering, OsloMet, Pilestredet 35, Oslo 0166, Norway
[f] Department of Aeronautics, Imperial College London, City and Guilds Building, South Kensington Campus, London SW7 2AZ, UK

ARTICLE INFO

Keywords:
Acoustic metamaterials
Active filtering
Core-shell structures
Controlling pass-/stop- bands
Magnetoelastomers

ABSTRACT

Acoustic metamaterials allow for creating selective pass- and stop-bands on the frequency spectrum. We demonstrate the possibility of designing acoustic metamaterials as core-shell 2D-phononic media with an extremely simple morphology, the frequency spectrum of which contains many real-time tunable bandgaps. The connected shells of such metamaterials form a grid with square cells filled with nuclei partitionable into two subsystems. Both subsystems are characterized by their frequency spectra, and it is the coupling between them that generates the bandgaps. If the structural elements of the metamaterial are built based on magneto-elastomers, then bandgaps can be easily controlled by an external magnetic field that changes the elastic moduli of shells/cores. We have shown the possibility of manipulating single bandgaps in different parts of the spectrum, and simultaneous control of all bandgaps up to their complete disappearance. This manipulation can be carried out, specifically, with no change in the maximum achievable frequency in the metamaterial. The results obtained can be used for selective filtering of damaging wave components, active control of seismic or blast waves, sonar systems, ultrasound imaging, impact-resistant structures, and noise cancelation protocols. The physical concepts developed are extendable to 3D-structures in a similar fashion so can benefit a wider community.

1. Introduction

Acoustic metamaterials possess synthetically designed micro-structures rendering possible manifestation of properties absent in natural materials [1–5]. The created artificial structures can implement non-traditional physical effects that have been achieved in the physics of electromagnetic and phononic metamaterials, for example, the negative refractive index of the medium [6,7], acoustic cloaking [8,9] or acoustic superlensing [10,11].The most prominent of these is the possibility of creation of pass- and stop-bands in the frequency spectrum by tuning system parameters [2,12,13]. Stop-bands or bandgaps, in the context of acoustic metamaterials, are defined as frequency intervals over which the excitation of phononic waves in the designed metamaterial is impossible. There are two distinguishable mechanisms responsible for the formation of bandgaps [14]. The first is related to the Bragg scattering of acoustic waves in the so-called phononic crystals [15–19]. In this case, wave interference forms a high-frequency bandgap, the characteristic wavelengths of which are determined by the period of the created ordered structure. Thus, the first mechanism is not suitable for suppressing low-frequency waves [20–22]. The second mechanism is associated with embedding an ordered structure of local resonators in an elastic medium [23–27]. The bandgaps are then formed as a result of the antiphase motion of the resonators relative to impact of the external elastic medium surrounding them [28–32]. The bandgap is determined by the resonant frequencies of the resonators, a phenomenon which makes such media suitable for suppressing low-frequency waves [33–36]. Numerous applications are based on this property of "resonant" metamaterials: vibration suppression [37–42], stress wave amplitude reduction [25,43], and seismic isolation [44–47] to name a few.

* Corresponding author at: Department of Mechanical, Electronic and Chemical Engineering, OsloMet, Pilestredet 35, Oslo 0166, Norway.
E-mail address: arashsol@oslomet.no (A.S. Fallah).

https://doi.org/10.1016/j.ijmecsci.2022.107829
Received 18 July 2022; Received in revised form 29 September 2022; Accepted 7 October 2022
Available online 8 October 2022

In turn, the successful solution of the problems of practical use involving acoustic metamaterials requires the development of methods for generating a controlled spectrum of propagating acoustic waves [17,48–52]. The conventional designs of metamaterials rely on 'passive' systems of predefined geometry, topology, and mass and stiffness distributions achieving the goal of the creation of bandgaps [53,54]. Active systems that form a controlled set of bandgaps by actively changing the parameters of these systems have wider applications and create greater opportunities in the creation of multifunctional acoustic devices through lifting the 'passiveness' restriction.

Solutions to the problem above are found in different ways including using directional-dependent stiffness elements (anisotropic metamaterials) [1,12,55], multivibrator systems with the so-called mass-in-mass structures (in which the central nucleus is covered by several nested shells similar to a Matryoshka doll [13,56]), labyrinthine [57–59], chiral [60–61], or fractal/pseudo-fractal microstructures [55,62,63]. There are several mechanisms which may assume the responsibility for the transition between passive and active metamaterials [51,64,65]. These include active alteration of stiffness or inertial elements in the medium or at the location of nodes, among others [9,66–68].

The real-time solution to the problem of controlling the set of bandgaps in resonant metamaterials faces the following physical complexity. The boundaries of the bandgaps, as noted above, are determined by the resonant frequencies of the resonators/nodes of the lattice. Therefore, a change in the parameters of the medium in which an ordered system of nodes is immersed does not significantly change the frequency ranges of these gaps. Changing the parameters of the resonators will simply shift the boundaries of the bandgaps, which excludes the possibility of changing the number of bandgaps up to their complete disappearance.

In this paper, we present the physical principles based on which, in structures that are quite simple in topology, the possibilities of controlling the formation of bandgaps can be significantly expanded. In these structures, there is no clear division of composite elements into a system of resonators and their external environment. The characteristics of the acoustic properties of the material are controlled by an external magnetic field that changes the stiffness of elements in the entire acoustic system, created on the basis of magnetorheological elastomers.

Magnetorheological elastomers (MREs) are smart composite materials whose mechanical and rheological properties are changed by an external magnetic field [69–72]. A typical MRE is a result of the dispersion of micro-sized magnetic particles in a non-magnetic polymer matrix such as natural rubber, silicone rubber, polyurethane, or several thermoplastics [73–76]. In an alternative external magnetic field, the interaction between magnetic particles rapidly (in a time range counting up to several milliseconds [77]) and reversibly [78,79] changes the elastic modulus and damping properties of the MRE tracking the variations of the magnetic field's strength. The ability to control an MRE's properties almost in real time [80] is used in numerous engineering applications, such as vibration dampers [81,82], vibration isolators [85–87] vibration control and mitigation [83–85], actuators and sensors [86–88], engine mounts for a car [89], adaptive stiffness devices [72,90] and soft continuum robots [91,92].

The presented paper is organized into the following sections. Following this terse introduction, in Section 2 the basic physical concepts of the problem solved are discussed. In Section 3 the governing equations are derived, and the numerical model and the procedure of construction of the dispersion equation are presented. In Section 4 the equations are solved, and the results obtained are analyzed. Section 5 presents conclusions.

2. Basic concepts and formulation of the problem

We should note that the physical principle leading to the formation of bandgaps in ordered lattices is rather transparent. One of the conclusions of the mathematical treatment of systems like the one analyzed in the following may be expounded as such: the system of bandgaps in a medium composed of *n*-type multivibrators (where the nucleus is surrounded by *n*shells of different masses and layers with different elastic constants in between the masses) depends only on the listed characteristics of the internal structure of the nodes and is not contingent upon the characteristics of the substratum i.e. the medium in which the created lattice of nodes is embedded. Moreover, the set of bandgaps $\{\Delta\omega_{(i)}^2\}$, $i = 1, 2, 3, \ldots n$, does not depend on the type of symmetry of the created 'crystal' lattice.

In the sequel, we demonstrate the ground for the aforementioned statement using the example of a simple vibrator consisting of a nucleus, a shell ($n = 1$), and the internal elastic medium between them with the effective stiffness κ_i, i.e. a single resonator. The one-dimensional dynamics of this node under the action of an external force that depends only on time, $f(t) = f_0 e^{i\omega t}$, changes drastically in the case when the periodic force acting on the shell depends on the coordinates, x_e, of the shell itself: $f(t) = -Kx_e(t)$. In the first case, the solution of the system of equations of motion i.e.,

$$M\ddot{x}_e = \kappa_i(x_i - x_e) + f_0 e^{i\omega t},\ m\ddot{x}_i = \kappa_i(x_e - x_i), \tag{1}$$

for the displacements of the shell, $x_e = x_{eo}e^{i\omega t}$, and the core, $x_i = x_{io}e^{i\omega t}$, exists in the continuous frequency spectrum:

$$x_{eo} = \frac{f_o}{M}\frac{\omega_0^2 - \omega^2}{\omega^2\left(\omega^2 - \omega_f^2\right)}, x_{io} = \frac{f_o}{M}\frac{\omega_0^2}{\omega^2\left(\omega^2 - \omega_f^2\right)}, \tag{2}$$

where $\omega_0^2 = \kappa_i/m$ is the frequency of oscillations of the internal nucleus in the supposed case when the shell is rigidly fixed (moveless), $\omega_f^2 = \kappa_i/\widehat{m}$ is the eigen frequency of the isolated node, and the parameter $\widehat{m} = Mm/(M+m)$ is the reduced mass of the node ($\omega_f^2 > \omega_0^2$).

It is physically clear, that the oscillations of the core at low frequencies, $\omega^2 < \omega_0^2$, are in phase with the oscillations of the shell, i.e.

$$\xi = \frac{x_{eo}}{x_{io}} = 1 - \omega^2 \Big/ \omega_0^2 > 0, \tag{3}$$

when the ***effective*** stiffness, κ_i^*, of the internal medium of the node decreases. To excite high-frequency oscillations, $\omega^2 > \omega_0^2$, the value of κ_i^* must be higher than the stiffness κ_i, $\kappa_i^* > \kappa_i$, which is realized with antiphase displacements of the core and shell, $\xi < 0$ (see Eq. (3)). We note that in the case under consideration, for each equivalent stiffness, $K^*(\omega)$, of the external environment,

$$K^*(\omega) = -\frac{f_0}{x_{e0}} = M\frac{\omega^2\left(\omega_f^2 - \omega^2\right)}{\omega_0^2 - \omega^2}, \tag{4}$$

only one type of oscillation (either in-phase or in-antiphase) can be excited.

The situation changes drastically in the case of dependence of the external force on the coordinates of the shell, $f(t) = -Kx_e(t)$. Such dependence enhances the coupling between the shell vibration modes in the field of the elastic external environment and in the elastic internal medium of the node. This increased coupling induces an effect that is a classical analogue of quantum level splitting. In the situation under consideration, the splitting is due to a combination of the two oscillation modes above in both in-phase and anti-phase regimes. Accordingly, for each stiffness value, K, oscillations at two different frequencies are excited with the formation of a bandgap between the two corresponding branches $\omega^2 = \omega_{upper/lower}^2(K)$. The bandgap boundaries are easy to determine based on Eq. (4). In the frequency range of:

$$\omega_0^2 < \omega^2 < \omega_f^2 \tag{5}$$

the equivalent stiffness, K^*, is negative, $K^*(\omega) < 0$. Since the real value of

the stiffness of the external environment,K, is positive, then oscillations in such a frequency range are impossible. The result obtained from relation (4) is consistent with the exact solution of the problem for two oscillation branches, $\omega^2 = \omega^2_{lower}(K)$ and $\omega^2 = \omega^2_{upper}(K)$ as:

$$\omega^2_{upper} = \frac{1}{2}\left(\omega_f^2 + \Omega^2 + \sqrt{\left(\omega_f^2 + \Omega^2\right)^2 - 4\Omega^2\omega_0^2}\right) \geq \omega_f^2 \tag{6}$$

$$\omega^2_{lower} = \frac{1}{2}\left(\omega_f^2 + \Omega^2 - \sqrt{\left(\omega_f^2 + \Omega^2\right)^2 - 4\Omega^2\omega_0^2}\right) \leq \omega_0^2, \tag{7}$$

where $\Omega^2 = K/M$.

Relations (5)–(7) are obtained for an isolated node. If these nodes form a lattice in an external elastic medium, then the value of K in the equations of motion for an imaginary isolated node depends on the motion of the nodes of its immediate environment, i.e. from the excited wavelength. Thus, acoustic waves cannot propagate in the phononic metamaterials within the bandgap of Eq. (5), which is formed by only the structure of the isolated node.

In particular, waves of infinite wavelength, λ (wave vector $= \frac{2\pi}{\lambda} = 0$), correspond to oscillations of shells of nodes in antiphase with vibrations of nuclei in them without deformations of the external environment. Therefore, the upper limit of the bandgap coincides with ω_f^2, since in Eq. (6) the value Ω^2 should be considered equal to zero. Frequencies $\omega^2 < \omega_0^2$ correspond to in-phase oscillations of the shell and nucleus. From qualitative considerations, it is clear that the maximum achievable oscillation frequency in this case corresponds to the minimum amplitude of shell oscillations: $\omega^2 \to \omega_0^2$ at $x_{e0} \to 0$. Formally, the same result for the lower boundary of bandgap can be obtained by Eq. (7): $\omega^2_{lower} = \omega_0^2$ for $\Omega^2 \to \infty$.

When nodes are multivibrators of the n -type, the guaranteed bandgap boundaries are determined by the set of eigenfrequencies $\{\omega^2_{f(i)}\}$ and $\{\omega^2_{0(i)}\}$ as discussed in great detail in one of authors' previous works [13] (where the values $\omega^2_{0(i)}$, $i = 1, 2, \ldots n$, are calculated with the outermost shell as motionless).

Thus, the method of formation of bandgaps discussed above is 'passive' in the sense that it practically excludes the possibility of controlling the parameters of these gaps in real-time by changing the parameters of the medium in which the multivibrators are immersed. The only possible option is to change the elasticity of the spacers between the internal shells, which is not easy to implement technically.

In this paper, we consider another possibility for creating an 'active' i.e. time-controlled series of bandgaps. In the proposed version, either the single (see Fig. 1(a)) or coupled dual strings of red masses and red springs (see Fig. 1(b)) form shells of the adjacent elastic square cells. These shells themselves possess vibrational eigenmodes, in contradistinction to the rigid shells of the multivibrator systems mentioned above [13]. The internal content of the cells ('green'/'blue' masses and elastic medium represented by the system of green springs) is also characterized by its set of vibrational modes. The interaction of shells with internal 'multivibrators' may generate a system of bandgaps. At the same time, it becomes possible to change the elastic characteristics of both red shells and green multivibrators by an external magnetic field [93–98] and, accordingly, open/close individual frequency bands for passing or shift them up or down along the frequency scale. To implement such an idea, one can use magnetorheological elastomers (MRE) which are essentially composite materials capable of demonstrating significant changes in their physical properties under the influence of an external magnetic field - in particular, a significant increase in the moduli of elasticity of the material in sufficiently moderate magnetic fields of the order of 50~600 mT. As an example, in a magnetic field with an induction of 500 mT, elastomers containing carbonyl iron particles showed an increase in the elastic modulus by a factor of 277 [93,94].

MREs are made by adding iron powder and/or other additives to a liquid polymer material. The characteristics of the MRE, as particulate composites, are determined by the type of filler [95–97], the size of the particles [95], the volume fraction of the particles and their arrangement in the matrix [96,98]. In particular, the ordering of magnetic particles inside the polymer matrix at the stage of material curing makes it possible to obtain anisotropic samples [98]. The so-called bimodal MREs [95] consisting of both magnetic and non-magnetic particles demonstrate a greater increase in moduli of elasticity in a magnetic field of 320 mT than monomodal materials made only of magnetic particles. Since a magnetic field is a convenient control factor, the use of MREs in technology as a constituent or component in smart materials [99,100] is very promising. In the sequel, we expound the formulation of the problem, mechanisms of bandgaps formation in the MRE-based acoustic metamaterials, and principles of tuning with frequency-surfaces, $\omega_i^2 = \omega_i^2(\boldsymbol{k})$, within a fixed frequency range $0 < \omega^2 < \omega^2_{max}$.

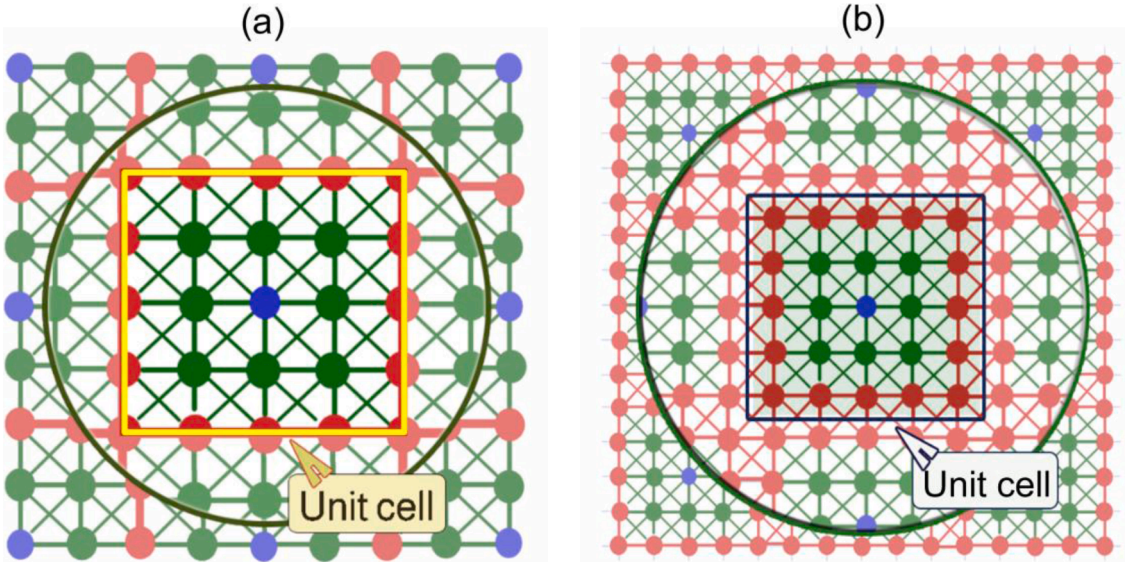

Fig. 1. Models of 2D multi-gaps acoustic systems comprised of adjacent elastic square cells of nucleus-shell type: (a) the shells are formed with single strings; (b) formation of the shells by dual coupled strings.

3. Model parameters and construction of the dispersion equation

Let us briefly describe the method for obtaining the initial dispersion relation using the example of a two-dimensional lattice shown in Fig. 1 (a). The unit cell of such a lattice contains seven (7) red nodes, eight (8) green nodes and one (1) blue node. The total number of nodes is thus 16, and the motion of each of them is characterized by displacements along the X- and Y-axes (along the horizontal and vertical directions). We denote the masses of these nodes in accordance with their color, as: m_r, m_g,and m_b. Red springs are characterized by stiffness κ_r. The stiffness of vertical and horizontal green springs is equal to $\kappa_g^{'}$, and the stiffness of inclined green springs, $\kappa_g^{''}$, which is assumed inversely proportional to their length: $\kappa_g^{''} = \kappa_g^{'}/\sqrt{2}$.

The general form of the desired dispersion equation is then as follows:

$$\boldsymbol{A}\boldsymbol{u} = \omega^2\boldsymbol{u} \tag{8}$$

where $\boldsymbol{u}$ signifies the displacement vector i.e. the transposed column vector of $\boldsymbol{u}^T = (\boldsymbol{x}^T,\boldsymbol{y}^T)$, where, $\boldsymbol{x}^T = (x_1,x_2,x_3,\ldots, x_{16})$, and $\boldsymbol{y}^T = (y_1,y_2,y_3, \ldots, y_{16})$. The sets $\{x_i\},\{y_i\}$ represent the displacements of the main lattice nodes (these nodes lying inside the square shown in Fig. 2 and numbered with yellow labels). Matrix $\boldsymbol{A}$ is a square matrix of dimensions 32×32 and is composed of the coefficients of the equations of motion for these nodes. When constructing these equations, it will be necessary to take into account the displacements of nodes lying outside the square in Fig. 2 (numbered with white labels).

Each of these auxiliary nodes is equivalent to a main node, and the displacements of equivalent nodes are related to the displacements of main nodes by Bloch's theorem (also known as 'Floquet-Bloch's principle' which asserts the fact that the change in the complex amplitude of a wave across a unit cell in an infinite lattice is independent of its position). For example, a primary node with the index 4 has three equivalent nodes in the directions North, North-East, and East, respectively, therefore:

$$\boldsymbol{u}_4^N = \boldsymbol{u}_4\exp\left(ik_y a\right),\ \boldsymbol{u}_4^{NE} = \boldsymbol{u}_4\exp\left(ik_y a + ik_x a\right),\ \boldsymbol{u}_4^E = \boldsymbol{u}_4\exp(ik_x a), \tag{9}$$

where $a = 4d$ is the unit cell size (d is the minimum distance between nodes), and $\boldsymbol{k} = (k_x,k_y)$is the wave vector of the plane acoustic wave.

Considering the small-amplitude harmonic vibration of node n i.e. its small oscillations around the equilibrium position, $\boldsymbol{u}_n = \boldsymbol{u}_{n0}exp(i\omega t)$, the equation of its motion, $m_n\ddot{\boldsymbol{u}}_n = \boldsymbol{f}_n$ takes the following form:

$$-\boldsymbol{u}_{n0}\omega^2 = \sum_{i=1}^{8}\boldsymbol{e}_i\left(\frac{k_i}{m_n}\right)\ (\boldsymbol{e}_i.(\boldsymbol{u}_{i0} - \boldsymbol{u}_{n0})) \tag{10}$$

The summation in (10) is carried out in eight directions from the central, n-th, node to the lattice nodes surrounding it. The vectors $\{\boldsymbol{e}_i\}$ are unit vectors oriented along these directions, $\boldsymbol{u}_{i0}$-the amplitudes of oscillations of the nodes, which are in general complex, and κ_i the stiffness coefficients of the corresponding springs. The dependence of the matrix $\boldsymbol{A}$i.e. its entries (formed from the coefficients of sixteen equations of the form (10)) on the dimensionless wave vector, $\widehat{k} = 2\pi a/\lambda$ in Eq. (10) is a consequence of applying Bloch's theorem to deviations at equivalent lattice nodes.

There are several options for the numerical procedure leading to the computation of the entries in matrix $\boldsymbol{A}$. Due to space constraints, however, we shall not describe the technical details of the algorithm we have devised and implemented here and will focus merely on the physical analysis of the results obtained.

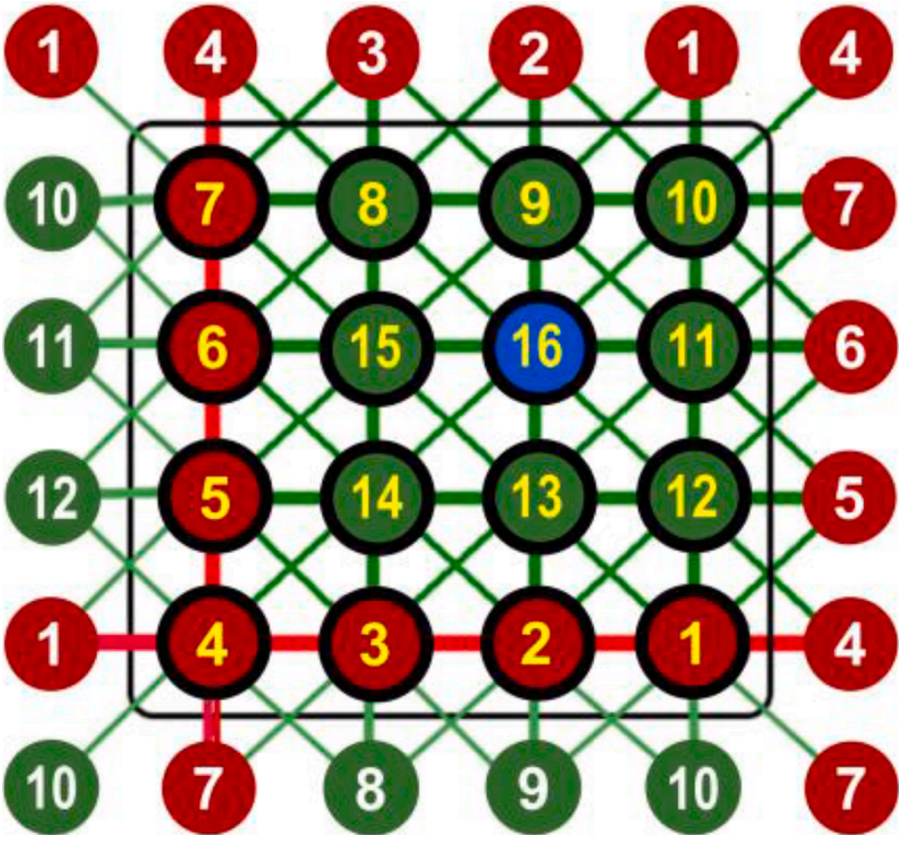

Fig. 2. The system of main and auxiliary (equivalent) lattice nodes used to construct the dispersion equation. The equations of motion are compiled for the main nodes lying inside the square bounding the primitive cell. The red and green segments indicate 'springs', which represent the interactions between the nodes that are taken into account when constructing these equations.

Dispersion surfaces have the form $\omega^2 = \omega_m^2(\widehat{\boldsymbol{k}})$, $m = 1, 2, 3, \ldots, 32$, which are considered over the first Brillouin zone, i.e.:

$$-\pi \le \widehat{k}_x \le \pi, \ -\pi \le \widehat{k}_y \le \pi \tag{11}$$

If we take into account the symmetry of dispersion surfaces $\omega^2 = \omega_m^2(\widehat{\boldsymbol{k}})$, then it suffices to study their morphology over the irreducible Brillouin zone i.e. the region $0 \le \widehat{k}_{x,y} \le \pi$.

Concerning the parameters of the system under consideration, in a similar fashion to dimensional analysis we assume the mass of the red nodes,m_r, to be unity. In this case, we have four independent parameters:

$$m_g, m_b, \omega_{rr}^2 = \kappa_r/m_r = \kappa_r \ , \omega_{gg}^2 = \kappa_g/m_g \tag{12}$$

The parameters in the sequel give the remaining quantities necessary for constructing the matrix $\boldsymbol{A}$:

$$\omega_{gr}^2 = \kappa_g/m_r = m_g \ \omega_{gg}^2, \text{and } \omega_{gb}^2 = \kappa_g/m_b = m_g \ \omega_{gg}^2/m_b \tag{13}$$

The dispersion equation for the two-dimensional system shown in Fig. 1(b) is analogically built on the basis of the equations of motion for 25 main nodes framed by 24 auxiliary/equivalent nodes. The set of 50 dispersion surfaces $\{\omega_m^2(\widehat{\boldsymbol{k}})\}$, presents the solution of the equation of motion, where the dimensionless wavevector $\widehat{k}$ equals $10\pi d/\lambda$.

4. Results and discussion

In Section 2, we considered the mechanism for the formation of bandgaps in a system of multivibrators forming an ordered lattice structure in an external elastic medium (a multi-resonator phononic metamaterial). Bandgaps arise in the frequency ranges over which the frequency of natural oscillations, ω_n^2, of isolated multivibrators, ($n$being the number of the mode of natural oscillations ordered in the descending order), is equal to the frequency of acoustic waves, propagating in the external environment: $\omega_n^2 = \omega_n^2(\boldsymbol{k})$. If there is a connection between the effects of external and internal forces on the multi-vibrator shells, an analogue of the quantum effect of level repulsion is realized in the classical system, which leads to a break in the dependence $\omega^2 = \omega^2(\boldsymbol{k})$ with the formation of bandgaps (see [2] for a detailed discussion). In any case, each natural frequency of the isolated multivibrator, ω_n^2, generates a dispersion surface with a frequency $\omega_n^2 = \omega_n^2(\boldsymbol{k} = 0)$ at the center of the Brillouin zone. In the sequel, we will also compare the set of frequencies of an isolated unit cell, $\{\omega_n^2\}$, $n = 1, 2, 3\ldots, N$, with the set of frequencies at the center of the Brillouin zone, $\{\omega_m^2(k = 0)\}$, $m = 1, 2, 3\ldots, M$, of an integral acoustic system composed of an infinite number of these cells, which interact with each other. Note that in the general case $N > M$. So, for the elementary cell shown in Fig. 1(a), $N = 50$ (25 constituent masses each possessing two degrees-of-freedom). In an integral system (Fig. 2), nonetheless, the number of independent degrees-of-freedom is reduced to $M = 32$.

The acoustic systems considered in this paper are composed of multivibrators with many degrees-of- freedom where green cores are enclosed in red shells. In this case, the concept of an elastic environment in which single multivibrators are immersed is irrelevant, since their 'environment' or 'ambience' is formed by adjacent multivibrators of the same structure. The direct interaction of neighboring 'green nuclei' by means of flexible 'red shells' separating them leads to the fact that in the general case the sets of frequencies $\{\omega_n^2\}$, and $\{\omega_m^2(k = 0)\}$ contain the restricted number of elements close in value. A measure of the interaction between green nuclei and red shells can be demonstrated quite easily. It is to this end that we calculate the sets $\{\omega_n^2\}$, and $\{\omega_m^2(k = 0)\}$ for different values of the quantity ω_{rr}^2 with other parameters fixed and analyze the changes in $\Delta\omega_n^2(\omega_{rr}^2)$ and $\Delta\omega_m^2(k = 0; \omega_{rr}^2)$ for different frequency ranges. Based on the magnitudes of these changes, it is possible to draw conclusions about the degree of correlation between the dynamics of elastic green cores and the rigidity of red shells both within the elements of an isolated cell and in collective processes characteristic of the integral medium.

Naturally, the control of pass- or stop-bands is possible only with a significant level of such mutual 'nuclei-shell' influence. As it will be denoted in the following sections, the results of the studies conducted show that a required level of correlations may be controllably achieved in selected areas of the frequency range for the acoustic system. Let us give a number of specific examples illustrating the statement above and demonstrating the physical principles of controlling bandgap gates.

4.1. Controlling bandgap gates in the low-frequency range of the spectrum

We shall not consider here the trivial case, in which all the stiffness coefficients of the acoustic system are changed by the same factor of η in an external magnetic field, and all bandgaps, if formed as such, will correspondingly shift along the frequency axis. Our goal is to control only the selected bandgaps without changing the rest of the gaps and to control the width of the overall frequency range. The rearrangement of the morphology of the set of dispersion surfaces in some frequency range is possible only in the case when it is in this range that the expressed coupling between vibrations of green cores and of red shells is realized. This requirement can be met by overlapping the characteristic frequencies of these two acoustic subsystems. When obtaining the results presented in Fig. 3, the selected parameters realize such an overlap only in the lower part of the spectrum, since for insignificant differences in the stiffness of red and green springs ($\kappa_r = \omega_{rr}^2 = 1.1 - 2.3, \kappa_g = \omega_{gg}^2 m_g = 1$), the mass of red nodes being five times the mass of green nodes. Thus, the spectrum of the subsystem of red shells is much narrower than that for green nuclei. This ratio can be easily estimated quantitatively.

With the selected parameters, the maximum frequency of acoustic waves, $\omega_{gr;max}^2$, which can be achieved in a two-dimensional system composed of green masses and springs is equal to:

$$\omega_{gr;max}^2 = 2\omega_{gg}^2\left(2 + \sqrt{2}\right) \approx 34. \tag{14}$$

A similar frequency, $\omega_{red;max}^2$, in a square system constructed only out of red horizontal/vertical springs and masses is:

$$\omega_{red;max}^2 = 4\omega_{rr}^2 \tag{15}$$

which lies in the range of 4.4 to 9.2. The estimates above explain why the changes in frequencies $\{\omega_n^2\}$ and $\{\omega_m^2(k = 0)\}$ with variations in the value of ω_{rr}^2 are observed (Fig. S3(a),(b)) at $n \ge 16$ (or $\omega_{n\sim}^2 \le 8$) - i.e. in the frequency range of acoustic waves that can be excited in a system composed only of red shells.

The apparently weakened coupling between green cores and red shells in the high-frequency part of the spectrum should also be expected to be reflected in the dynamics of the morphology of many surfaces $\omega^2 = \omega_m^2(\boldsymbol{k})$ with an increase in the stiffness of the red springs – see Fig. 4.

The initial bandgap structure is shown in Fig. 4 in two configurations, (a') and (a''), built for different frequency ranges (upper and lower). Note that the dispersion surfaces are represented by their sections cut by a plane passing through the straight line $k_x = k_y$. For such cross-sections, the gaps between adjacent curves quite often correspond to the actual bandgaps. Sometimes, as will be seen in the following figures, the actual width of the zone may be narrower than the gap between adjacent curves. In general, the selected graphical method of presenting the results obtained is quite informative for displaying the dynamics of multi-surface, $\omega^2 = \omega_m^2(\boldsymbol{k})$, acoustic systems.

Configurations (b), (c), and (d) in Fig. 4 show an unusual effect. The dispersion surface $\omega^2 = \omega_{16}^2(\boldsymbol{k})$ (marked with a green circle in Fig. 4, see configurations $((a'') - (d))$) remains practically unchanged with increasing ω_{rr}^2, and the lower surfaces $\omega_{17}^2(\boldsymbol{k})$ and $\omega_{18}^2(\boldsymbol{k})$, which are covered by a dashed ellipse, rise through it (surface number 16 becomes

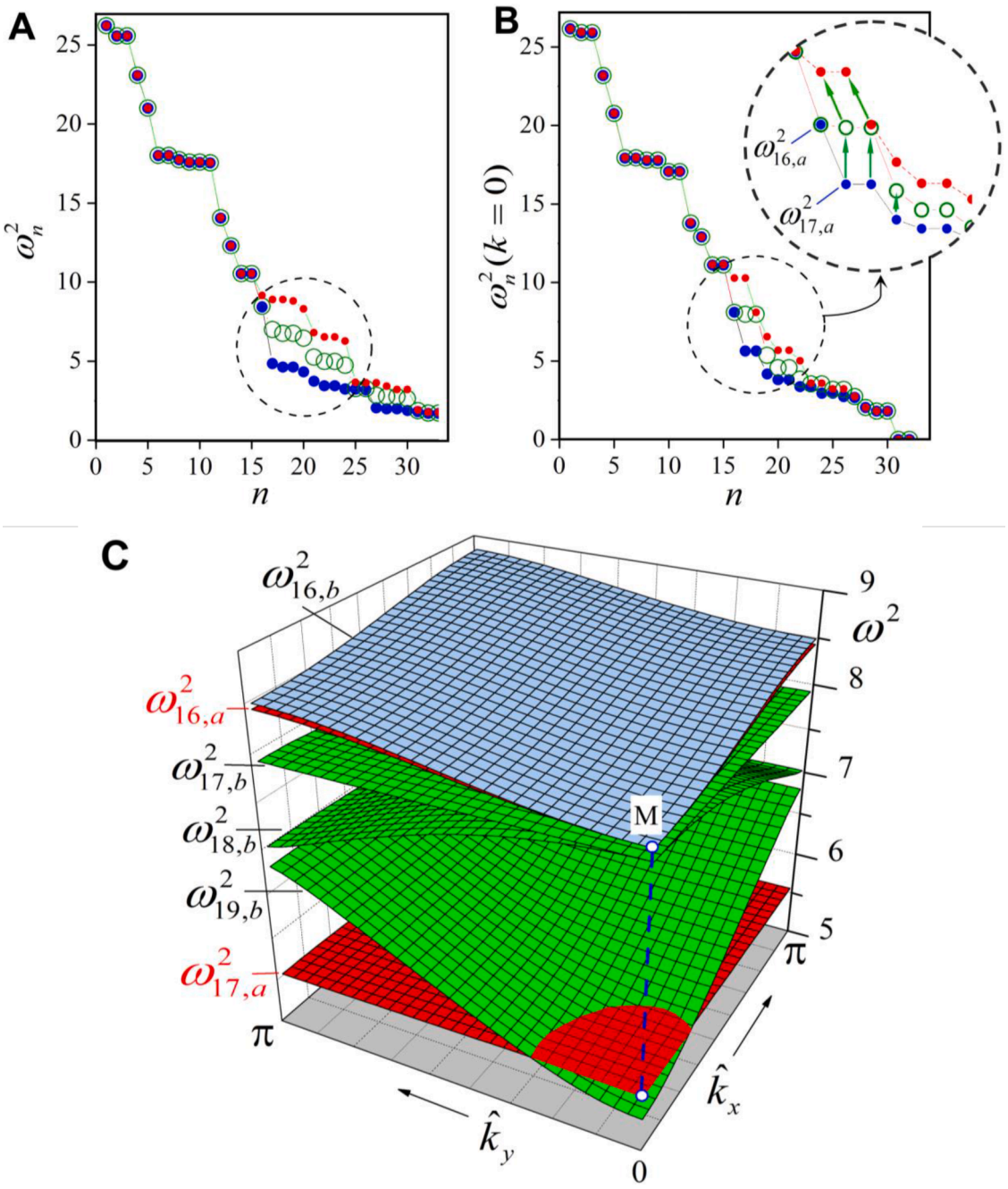

Fig. 3. Dynamics of dispersion surface morphologies through increasing the shells stiffness (red springs); $m_g = 0.2$, $m_b = 0.8$, and $\omega_{gg}^2 = 5.0$ (*n*is the number of frequency modes). (**A**) Sets of eigenfrequencies of the single unit cell: $\omega_{rr}^2 = 1.1$, 1.7, and 2.3 (blue, green, and red circles, respectively). (**B**) The set of eigenfrequencies of the entire acoustic system at $\boldsymbol{k} = 0$ for the same parameters as in subpart A. (**C**) Release of the lower band gap formed at $\omega_{rr}^2 = 1.1$, which is limited by dispersion surfaces marked in red $\omega_{17,a}^2(\boldsymbol{k})$ and $\omega_{16,a}^2(\boldsymbol{k})$ (also see Fig. 4(a'')), by shifted up $\omega_{19,a}^2(\boldsymbol{k})$, $\omega_{18,a}^2(\boldsymbol{k})$, and $\omega_{17,a}^2(\boldsymbol{k})$ dispersion surfaces at $\omega_{rr}^2 = 1.7$.

the 18th in a row) and gradually open the two lower bandgaps without changing the upper ones. Sharp changes in frequencies $\omega_{17}^2(\boldsymbol{k}=0)$ and $\omega_{18}^2(\boldsymbol{k}=0)$ are shown in the inset of Fig. 3(b) as pairs of green arrows. The shapes of the surfaces that open the passage of waves in the lower bandgap are shown in Fig. 3(c).

The physical basis for various degrees of coupling between green cores and red shells is demonstrated by the data provided in Fig. 5, which present the eigenvectors of Eq. (10). The displacements of the masses are shown in different vibration modes and for different stiffness values of the red springs. Modes with $m = 8$ and 16 that are resistant to variations in the ω_{rr}^2 parameter (see configurations (a) and (b) in Fig. 5) are characterized by a high degree of core mass mobility compared to the passive behavior of red/boundary masses, since these red masses are not able to track high-frequency oscillations of lighter green masses. Coupling sharply rises with decreasing modal frequency. An increase in the parameter ω_{rr}^2 from 1.1 to 2.3 leads to an increase in the frequency of a pair of degenerate modes, $\omega_{17}^2(k=0) = \omega_{18}^2(k=0)$, from 5.6 to 10.3 (after such an increase, this pair takes positions 16 and 17 in the set $\{\omega_m^2(k=0)\}$). The corresponding eigenvectors are characterized by intense horizontal oscillations of the red masses (see the upper and lower mass rows in configurations (c) and (d) of Fig. 5). Changing the frequency of oscillations in these rows directly reflects the increase in stiffness of the red springs. Intensive coupling in the core-shell system (between horizontal oscillations in neighboring vertical columns of red/

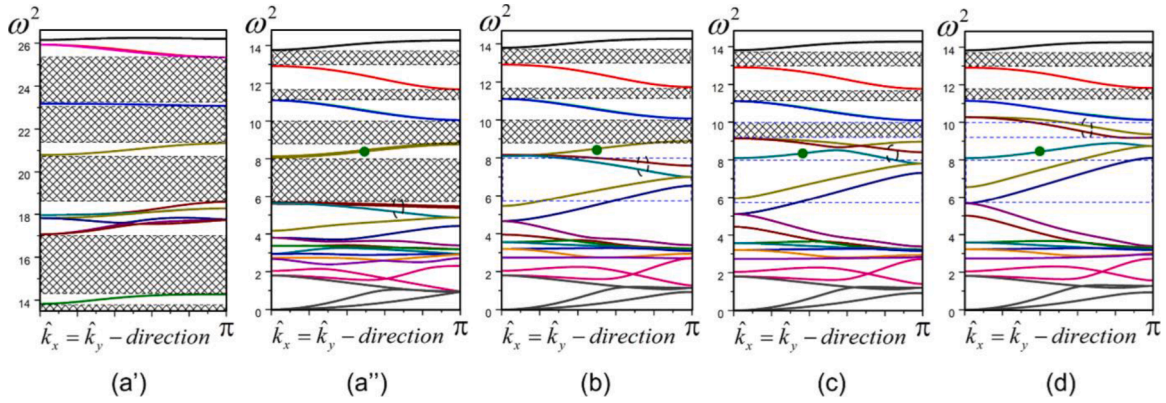

Fig. 4. Cross-sections of dispersion surfaces by the plane (1–10) in the(k_x,k_y,ω^2)-space; the dependencies $\omega^2 = \omega^2(0 \le k_x = k_y \le \pi)$ are presented. $m_g = 0.2$, $m_b = 0.8$, and $\omega_{gg}^2 = 5.0$. (a') and (a'') demonstrate these dependencies within upper ($14 \le \omega^2 \le 26$ -(a')) and lower ($0 \le \omega^2 \le 14$ -(a''')) frequency diapasons for $\omega_{rr}^2 = 1.1$. Configurations (b), (c), and (d) show controlled release of the bandgaps by increasing the stiffness of shells (red springs): $\omega_{rr}^2 = 1.75,\ 2.0,$ and 2.3, respectively.

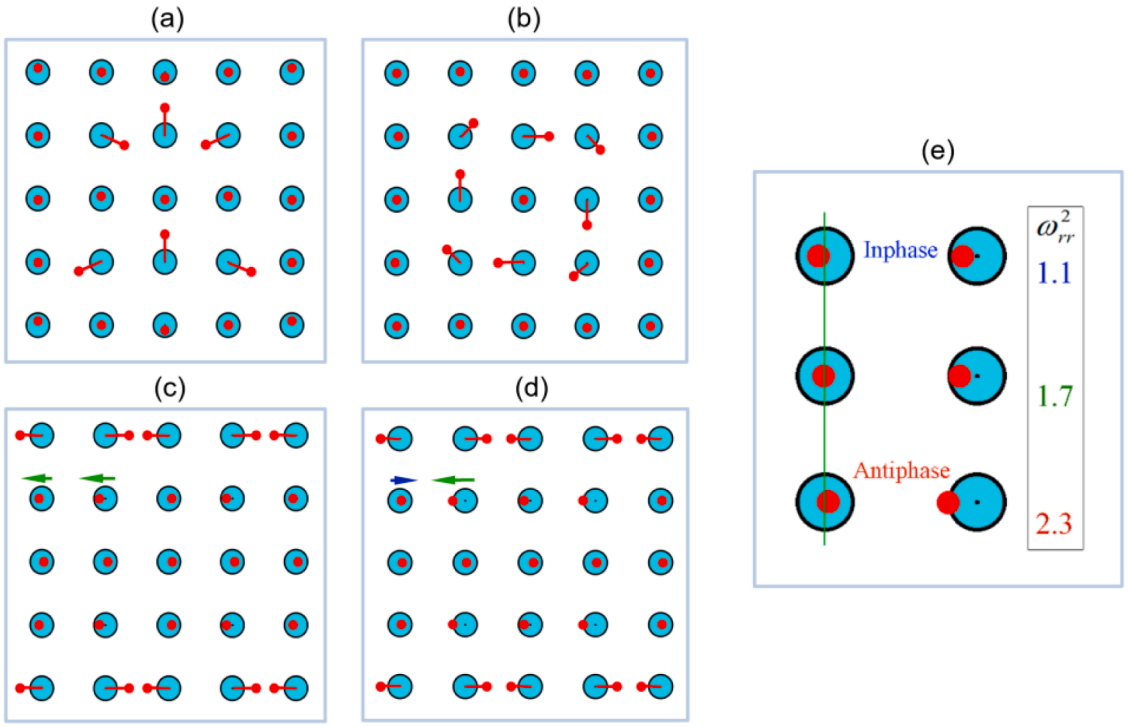

Fig. 5. Graphical representation of eigenvectors that characterize the acoustic system shown in Figs. 3 and 4: $m_g = 0.2$, $m_b = 0.8$, and $\omega_{gg}^2 = 5.0$. The initial positions of nodes coincide with centers of cyan circles, centers of displaced red circles represent amplitudes of their vibrations. For the small displacements to be more visible, the initial positions are enveloped by black circles. Configuration (a), (b), and (c): displacements of nodes for modes of $n = 8$, 16, and 17 at $\omega_{rr}^2 = 1.1$ ($\omega_8^2 = 17.795$, $\omega_{16}^2 = 8.093$, $\omega_{17}^2 = \omega_{18}^2 = 5.631$). Configuration (d): $\omega_{rr}^2 = 2.3$, displacements of nodes for the mode of $n = 16$ ($\omega_{16}^2 = \omega_{17}^2 = 10.274$, and $\omega_{18}^2 = 8.093$ - as the parameter ω_{rr}^2 increases, the pair of degenerate dispersion surfaces of $n = 17$ and 18 rises above the former dispersion surface of $n = 16$). Configuration (e) depicts the evolution of the phase-shift between oscillations of the pair of red-end green nodes, which are marked by arrows in configurations (c) and (d), when the stiffness ω_{rr}^2 increases.

green nodes) is less visually noticeable. Growth in the frequency of low-amplitude oscillations of the green nuclei is a result of increasing the effective stiffness of the green springs that connect these columns, which can be explained as follows.

We pay particular attention to a pair of neighboring red and green masses marked by arrows in Fig. 5(c) and (d). When the value of κ_r increases (recall that due to our choice of parameters $\kappa_r = \omega_{rr}^2$), the phase shift between relatively small oscillations of these masses is from 0 (see Fig. 5(c)) to π (see Fig. 5(d)). The transition from the in-phase mode of oscillations of these two masses to the anti-phase mode is repeated in configuration Fig. 5(e). With such a transition, the effective stiffness of the green springs connecting these masses increases, with a corresponding increase in the oscillation frequency. Thus, the strengthening of coupling manifests itself in the growth of correlations between the effective characteristics of the elasticity of multi-node 'shells' and multi-node 'cores'.

4.2. *Controlling bandgap gates in the high-frequency range of the spectrum*

It is desirable to have control over pass- and stop-bands for a wide range of frequencies i.e. not only low but also high-frequency compo-

nents of a given wave. To implement such control, it is necessary to choose system parameters such that, when varying the rigidity of the red shell, minimal changes in the morphology of dispersion surfaces in the low-frequency part of the spectrum with significant rearrangements of these surfaces in the high-frequency region is ensured. Based on the results of the previous section, consider a system with the following parameters: $m_g = 4.5$, $m_b = 1.5$, and $\omega_{gg}^2 = 1.2$; the frequency ω_{rr}^2 is changed in the range of 1 to 4. In this case, the cell cores are formed by heavy nodes and rigid springs ($\kappa_g = 5.4$). The maximum achievable frequency in such a system is:

$$\omega_{gr;max}^2 = 2\omega_{gg}^2\left(2+\sqrt{2}\right) \approx 8.2 \tag{16}$$

Similar frequency for a grid of red shells equals:

$$\omega_{red;max}^2 = 4\omega_{rr}^2 \approx 16 \tag{17}$$

Fig. 6 shows the expected result for the selected parameters. In contrast to the previous section, the eigenfrequencies of the system react very weakly to changes in the shell stiffness precisely at low frequencies.

The analysis of the results obtained above shows the large amount of information extracted out of graphical representations of the system's eigenvectors (solutions of Eq. (10)). As a rule, the low mobility of the masses of the red shell with a relatively active core indicates a weak core-shell bond, which leads to small variations in $\Delta\omega_n^2(\omega_{rr}^2)$ and $\Delta\omega_m^2(k=0;\omega_{rr}^2)$ when changing the value of ω_{rr}^2. In turn, the small variations $\Delta\omega_m^2(k=0;\omega_{rr}^2)$ slightly change the 'portraits' (graphical representations) of the corresponding eigenvectors. However, even in the case of noticeable shifts in the frequency of a certain mode, its portrait remains visually unchanged and easily recognizable among many similar portraits. Such an example is the configuration (a) of Fig. 7. It displays the eigenvector of mode $\omega_{16}^2(k=0;\omega_{rr}^2=1)$. Changes in the parameter ω_{rr}^2 from 0.8 to 4.0 increase the eigenvalue $\omega_{16}^2(k=0)$ from 6.435 to 12.181, but changes in the eigenvector portrait are visually imperceptible. Successive significant shifts in the 3D-space of the corresponding dispersion surface are presented in the curves pertaining to Fig. 8 which are marked with blue arrows.

Configurations (b), (c), and (d) in Fig. 7 show mode portraits that remain practically frequency-pinned at the center of the Brillouin zone (see three blue circles on the ω^2-axis in Fig. 8). Configuration (b) and its analogue rotated by $\pi/2$ represent a degenerate pair of the highest frequency dispersion surfaces ($\omega_{14,15}^2(k=0)$) - see Fig. 8(a)) from the marked trio of surfaces. Note that the high mobility of the shell elements should be understood as a 'relative' phenomenon i.e. the high mobility of these elements relative to each other. Therefore, the core-shell coupling in configuration (b) with pronounced in-phase shifts of red masses (see Fig. 7) is rather weak: the corresponding frequency at $k=0$ increases from 8.064 only to 8.208. Configuration (c) in Fig. 7 corresponds to the non-degenerate mode $\omega_{17}^2(k=0)=6.240$ in Fig. 8, which remains 'frozen' at this level as ω_{rr}^2 grows from 0.8 to 4. The most sensitive to changes in ω_{rr}^2 is the degenerate pair $\omega_{18,19}^2(k=0)$, whose portrait is given by configuration (d) in Fig. 7: $\omega_{18,19}^2(k=0,\omega_{rr}^2=0.8)=4.773$, and $\omega_{18,19}^2(k=0,\omega_{rr}^2=4.0)=5.036$.

Thus, the noticeable dynamics of dispersion surfaces in the upper part of the spectrum opens the bandgap gates in this frequency range, keeping these gates locked in the lower frequency range (see Fig. 8).

4.3. Strong broadband core-shell coupling

In the previous sections, we showed the possibility of controlling some bandgaps from the general set of bandgap gates formed – either in the lower (see. Fig. 4) or in the upper (see Fig. 8) part of the spectrum of acoustic waves. Note that varying the stiffness of the red shell did not change the maximum oscillation frequency achievable in the system (see Figs. 3(b) and 6(b)). In this section, we shall show the possibility of controlling the total set of initially formed bandgaps, and, again, without changing the width of the general frequency range. The result obtained is based on the following approximate physical concepts. The first of these is to reduce differences in the feature/structure of the green cores and red shells. For this, we use below shells composed of two coupled strands of red masses and springs (see Fig. 1(b)). Between the red masses, as between the green masses, inclined springs are inserted to more realistically replicate a continuous elastic medium lying in between the masses.

The second concept - the transformation to full transparency of all bandgaps should largely correspond to the transition of the morphology of the acoustic system from pronounced spatial structuring, which ensures the formation of bandgaps, to spatial quasi-homogeneity (it is

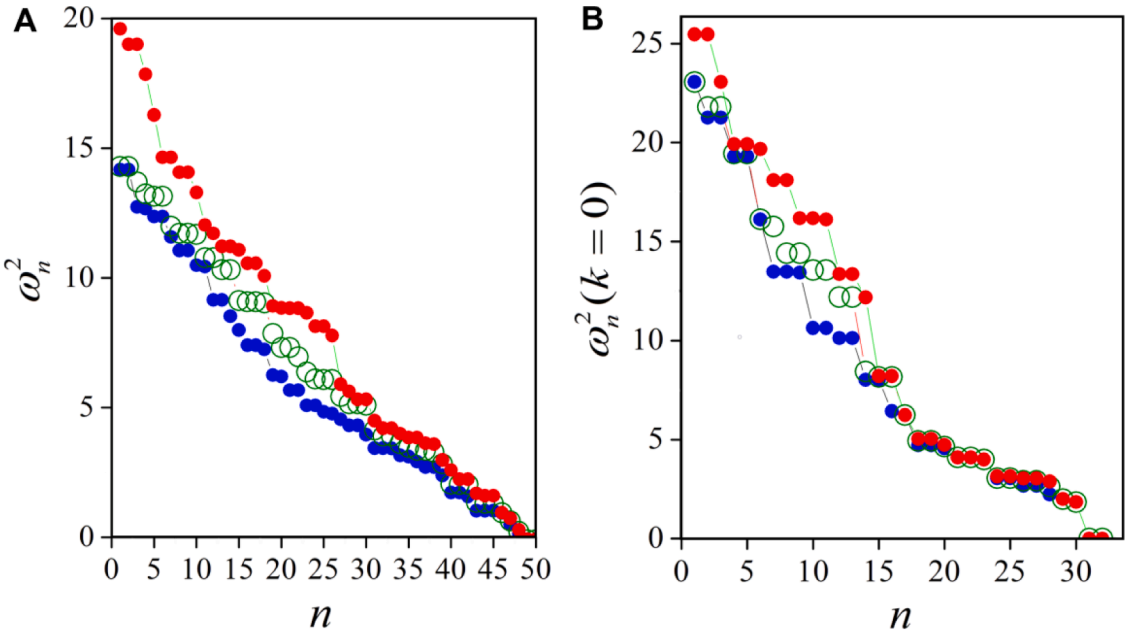

Fig. 6. (A) Eigenfrequencies of a single unit cell, $\{\omega_n^2\}$, and (**B**) eigenfrequencies of the entire acoustic system, $\{\omega_m^2(k=0)\}$, at $\omega_{rr}^2 = 0.8,\ 2.5,$ and 4.0 (blue, green, and red circles, respectively); $m_g = 4.5$, $m_b = 1.5$, and $\omega_{gg}^2 = 1.2$.

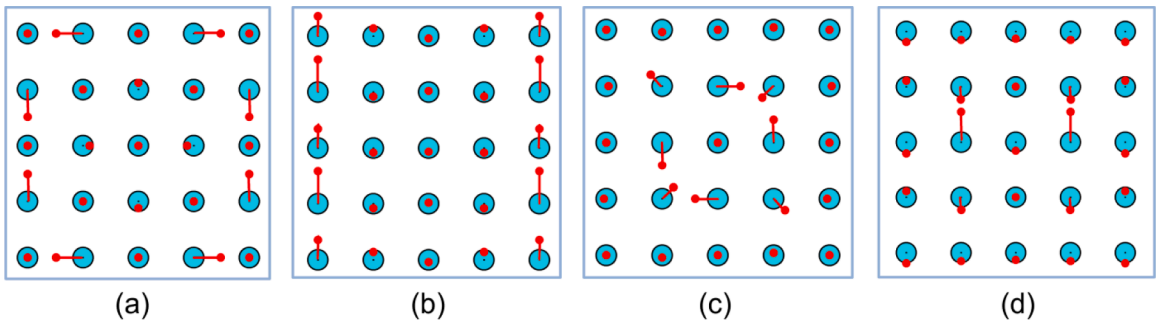

Fig. 7. Graphical representations of some acoustic system eigenvectors: $m_g = 4.5$, $m_b = 1.5$, $\omega_{gg}^2 = 1.2$, and $\omega_{rr}^2 = 1.0$. Configuration (a) represents the structure of the eigenvector of the most frequency-changing mode ($n = 16$ in Fig. 8(a) and (b), and $n = 14$ in Fig. 8(c), (d), and (e) - the marked by blue arrow curves). Configurations (b), (c), and (d) are portraits of modes 'frozen' in the low-frequency range (marked with blue circles in Fig. 8). The relative changes in the indicated frequencies, $\omega_m^2(k = 0)$, with the variation of the shell stiffness, ω_{rr}^2, from 0.8 to 4 are equal to 80%, 1.8%, 0.0%, and 5.5%, respectively.

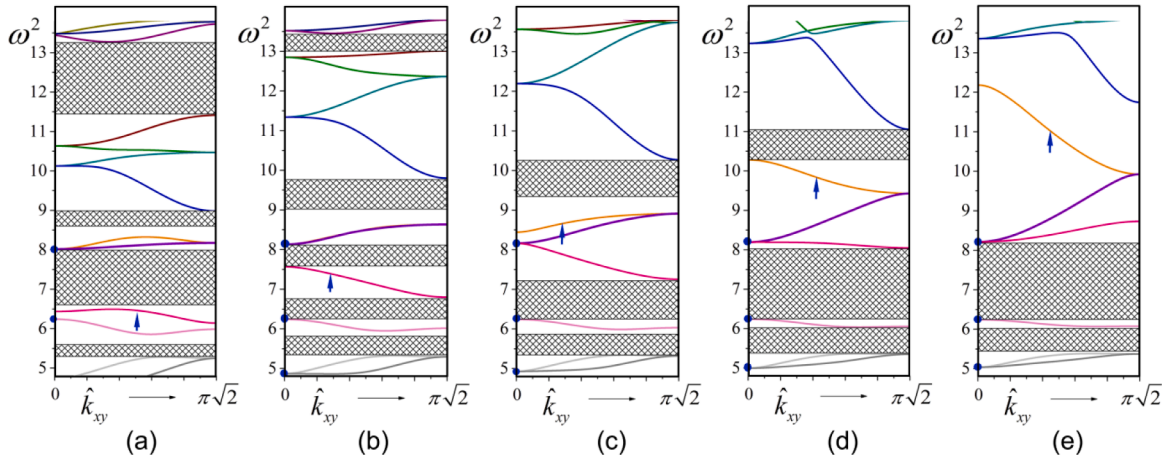

Fig. 8. Cross-sections of the dispersion surfaces by the plane (1–10) in the (k_x,k_y,ω^2)-space; the dependencies $\omega^2 = \omega^2(0 \le k_x = k_y \le \pi)$ are presented; $m_g = 4.5$, $m_b = 1.5$, $\omega_{gg}^2 = 1.2$. Configurations (a) - (e) show controlled release of the bandgaps at upper frequencies by increasing the stiffness of shells (red springs): $\omega_{rr}^2 = 0.8,\ 1.5,\ 2.0,\ 3.0,\ 4.0$, respectively.

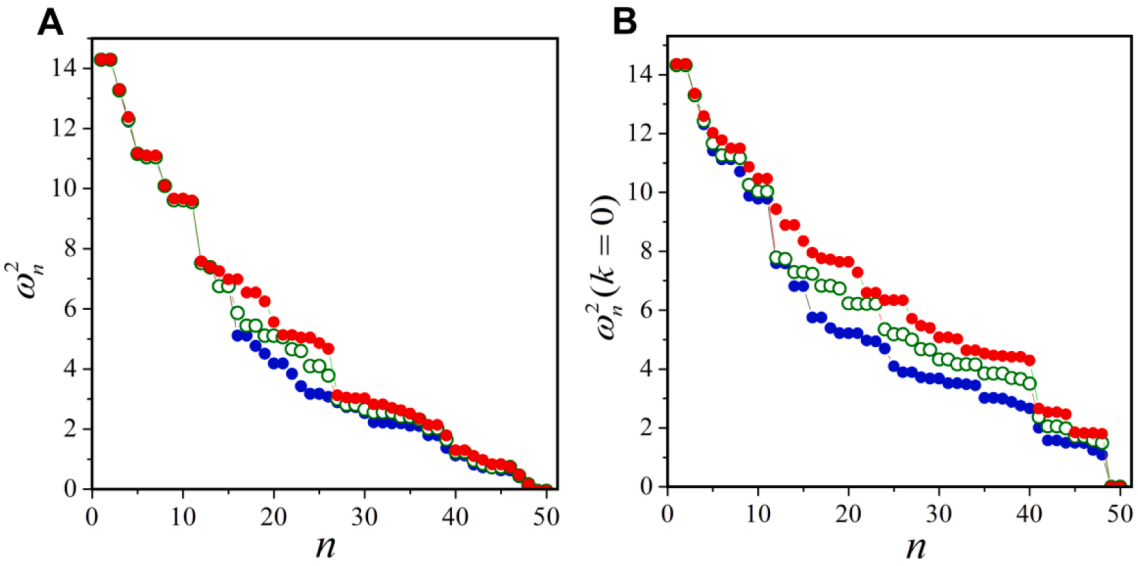

Fig. 9. (A) Eigenfrequencies of a single unit cell, $\{\omega_n^2\}$. (**B**) Eigenfrequencies of the entire acoustic system, $\{\omega_m^2(k = 0)\}$; $\omega_{rr}^2 = 0.8,\ 1.2,$ and 1.6 (blue, green, and red circles, respectively); $m_g = 0.7$, $m_b = 0.75$, and $\omega_{gg}^2 = 2.5$.

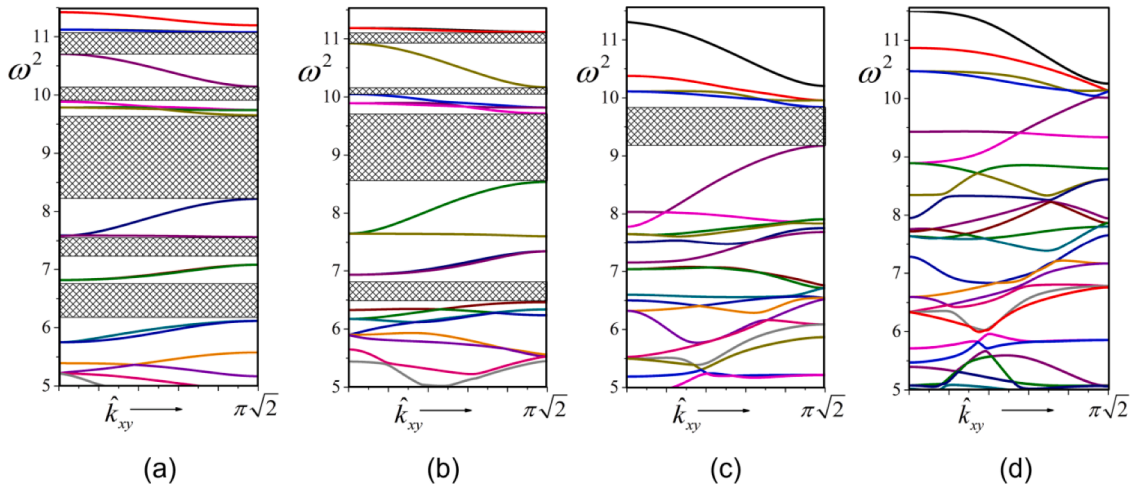

Fig. 10. Cross-sections of the frequency surfaces by the plane (1–10) in the (k_x,k_y,ω^2)-space; the dependencies $\omega^2=\omega^2(0\le k_x=k_y\le\pi)$ are presented; $m_g=0.7$, $m_b=0.75$, and $\omega_{gg}^2=2.5$. Configurations (a)-(d) show the controlled release of the band gaps by increasing the stiffness of shells (red springs): $\omega_{rr}^2=0.8,\ 1.0,\ 1.3,$ and 1.6.

obvious that there are no bandgaps in the acoustic system of equivalent nodes/springs).

The results obtained are displayed in Figs. 9 and 10. The system of equations of the form (4) is constructed for the coordinates of 25 independent nodes (nine nodes of the core complement and 16 red masses that cover this core along its perimeter - see Fig. 1(b)). In accordance with the stated physical concepts, the masses are chosen with a small deviation from their average value. The stiffness of the green springs is $\kappa_g=m_g\omega_{gg}^2=1.75$. Thus, with an increase in the parameter ω_{rr}^2 to a value of 1.6 (see Figs. 9 and 10), the acoustic system approaches the state of spatial homogeneity.

Let us note that this choice of parameters strengthened the coupling between cores and shells. To confirm this statement, it suffices to compare the data included in Figs. 3(a), 6(a), and 9(a) with the data presented in Figs. 3(b), 6(b), and 9(b), respectively. In each pair of figures, attention should be paid to how the distribution of frequencies $\{\omega_n^2\}$ obtained for different ω_{rr}^2, changes when compared with the corresponding distribution in the set $\{\omega_m^2(k=0)\}$. Since the green cores of the cells of the acoustic structure interact with each other through the mediation of red shells, the measure of difference in the distributions above is an indicator of the intensity of core-shell coupling over different frequency ranges with a variation in the elasticity of these shells. Visual assessment of the intensity of the coupling using the results of Fig. 9(a) and (b) suggests that this indicator significantly exceeds the same indicator obtained from a comparative analysis of the data presented in Figs. 3 and 6, both in magnitude and width of the frequency range.

The main result of such an increase in coupling is the complete disappearance of bandgaps (see Fig. 10) with a rather insignificant increase in the rigidity of the red shells (by a factor of two). Naturally, in the reverse process (lowering this rigidity), the gates of bandgaps will operate.

Analyzing the results obtained in Section 3, each time we could contemplate the entire acoustic system as a subsystem of green cores filling the cells of a square grid comprised of red masses and springs. The results of such a representation to perform approximate calculations quite satisfactorily predict the most general features of the dynamics of the entire system. However, the versatility of collective processes remains beyond the reach of such qualitative conceptions. This assertion is demonstrated by the data presented in Fig. 11.

In the acoustic system shown in Fig. 10, the mass of the central blue nodes was increased from 0.75 to 2. The eigenfrequency of the single vibrator, composed of the central blue mass and the outer shell of 8 green masses, is about 5, as this can be easily evaluated. Therefore, the rearrangements in the frequency range $\omega^2\sim$ 5–6 are physically clear

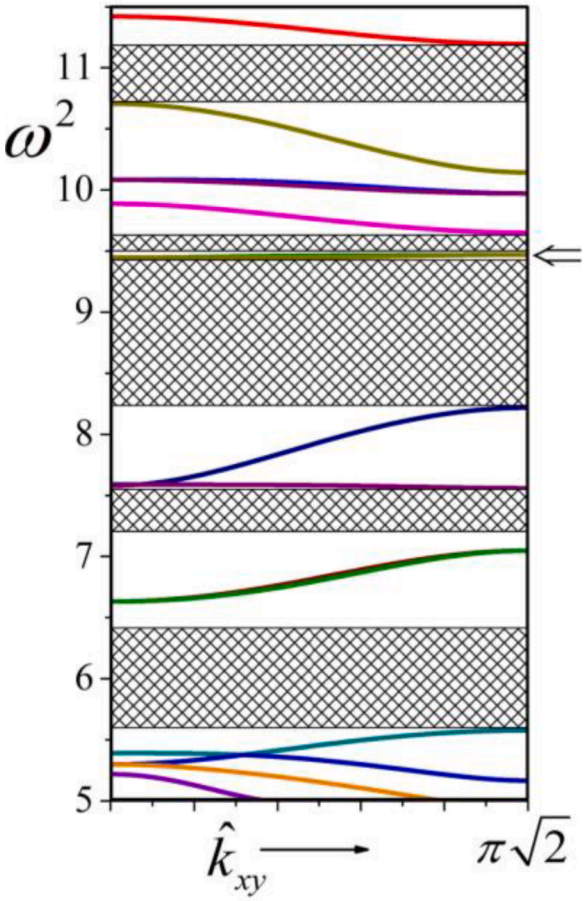

Fig. 11. Bandgaps and dependencies $\omega^2=\omega^2(0\le k_x=k_y\le\pi)$ in case of heavier blue masses: $m_b=2$. $\omega_{rr}^2=0.8$, the rest of parameters are the same as in Fig. 10.

when comparing the results shown in Figs. 11 and 10(a). However, morphological modifications in the interval $9\lesssim\omega^2\lesssim10.5$ associated with collective processes cannot be interpreted qualitatively. Nevertheless, the final result at $\omega_{rr}^2=1.6$ remains unchanged - in Fig. 10(a) all visible bandgaps become opened.

5. Conclusions

This paper concerns smart acoustic metamaterials capable of manipulating bandgaps through utilization of a magnetic field. The theoretical aspects on the manipulation of wave propagation in acoustic metamaterials using active pass- and stop-band generating mechanisms have been analyzed in the present work. The proposed method is to use magnetoelastic materials to render variable elastic moduli in the substratum. In real time, a significant rearrangement of the morphology of the set of acoustic surfaces $\{\omega_m^2(\boldsymbol{k}, \omega_{rr}^2)\}$ can be implemented in core-shell phononic metamaterials, the structural elements of which are magnetoelastomers.

The physical concepts of controlled opening-closing of the bandgaps are as follows. When altering the stiffness of the shells by a variable magnetic field, acoustic surfaces, $\omega^2 = \omega_m^2(\boldsymbol{k}, \omega_{rr}^2)$, shift/transform to varying degrees in the 3D space (k_x, k_y, ω^2) so that basic points/origins of those surfaces, $\{\omega_m^2(k = 0)\}$, 'mix' on the frequency axis, i.e. in the plane $(\omega^2, \omega_{rr}^2)$, some of the trajectories, $\{\omega^2 = \omega_m^2(k = 0, \omega_{rr}^2)\}$, intersect. On the one hand, it is the level of coupling between the cores and shells that determines the 'mobility' of each mode, $\Delta\omega_m^2(k = 0; \omega_{rr}^2)$, when varying ω_{rr}^2, which is essentially inhomogeneous in the mode number. On the other hand, it is this mixing that is responsible for opening/closing the gates of bandgaps/passage bands.

The geometry and parameters of the acoustic systems can be chosen so that:

- Noticeable variations in the elasticity of the shells by an external magnetic field practically do not change the maximum achievable wave frequency (see Figs. 3(b), 6(b), 9(b)), and the time-dependent processes of opening/closing gates of bandgaps occur in a controlled regime within a fixed frequency range being realized with a radical modification of just the morphology of the dispersion surfaces set $\{\omega_m^2(\boldsymbol{k}, \omega_{rr}^2)\}$.
- It is possible to create the most mobile modes, sensitive to changes in the shell stiffness, in the upper or lower region of the overall frequency range, so that a change in the morphology of the set of dispersion surfaces will be implemented only over a limited frequency range without a noticeable transformation outside it.

The developed concepts are quite realizable in applied developments since the necessary changes in stiffness of the shells (by a factor of 2–5 in the considered variants, which are much less than the increases already achieved of about 300 times) require insignificant variations in the external magnetic field. The lag in changes in the stiffness of magnetoelastomers, τ_{lag}, relative to variations of the magnetic field strength is quite small ($\tau_{lag} \sim$ several milliseconds), which opens up the possibility of smoothly changing the system of bandgaps in real time intervals, τ, that are much longer than τ_{lag}: $\tau \gg \tau_{lag}$. Since certain gaps are virtually untouched, the active control mechanism devised can be utilized in many applications for protection against damaging wave components, active control of seismic or blast wave propagation, ultrasound imaging protocols, and noise cancelation devices.

The physical concepts developed can be applied to 3D-structures in a similar fashion. Furthermore, the study opens the door to the possibility of achieving optimized solutions per application in the space of alternatives given certain set of constraints.

Data availability statement

The raw/processed data required to reproduce these findings cannot be shared at this time as the data also forms part of an ongoing study.

CRediT authorship contribution statement

Vyacheslav N. Gorshkov: Conceptualization, Methodology. **Oleksii V. Bereznykov:** Software, Writing – original draft. **Gernot K. Boiger:** Formal analysis, Supervision, Writing – original draft. **Pooya Sareh:** Validation, Visualization, Writing – review & editing. **Arash S. Fallah:** Conceptualization, Supervision, Investigation, Writing – original draft.

Declaration of Competing Interest

None.

Data Availability

Data will be made available on request.

Acknowledgment

The research presented in this paper was supported by the Swiss National Science Foundation (SNSF) under the Scientific Exchanges' Mobility Grant (Grant No.: IZSEZ0_206111).

References

[1] Fallah AS, et al. Wave propagation in two-dimensional anisotropic acoustic metamaterials of K4 topology. Wave Motion 2015;58:101–16.
[2] Gorshkov VN, Navadeh N, Fallah AS. A study of frequency band structure in two-dimensional homogeneous anisotropic phononic K-3-metamaterials. Smart Mater Struct 2017;26(9):095058.
[3] Huang HH, Sun CT, Huang GL. On the negative effective mass density in acoustic metamaterials. Int J Eng Sci 2009;47(4):610–7.
[4] Sharma B, Sun CT. Local resonance and Bragg bandgaps in sandwich beams containing periodically inserted resonators. J Sound Vib 2016;364:133–46.
[5] Zhang S, et al. Cloaking of matter waves. Phys Rev Lett 2008;100(12):123002.
[6] Fleury R, Alu A. Extraordinary sound transmission through density-near-zero ultranarrow channels. Phys Rev Lett 2013;111(5):055501.
[7] Smith DR, Pendry JB, Wiltshire MC. Metamaterials and negative refractive index. Science 2004;305(5685):788–92.
[8] Zhang S, Xia C, Fang N. Broadband acoustic cloak for ultrasound waves. Phys Rev Lett 2011;106(2):024301.
[9] Cummer SA, Christensen J, Alù A. Controlling sound with acoustic metamaterials. Nat Rev Mater 2016;1:16001.
[10] Li J. Experimental demonstration of an acoustic magnifying hyperlens. Nat Mater 2009;8:931–4.
[11] Zigoneanu L, Popa BI, Cummer SA. Design and measurements of a broadband two-dimensional acoustic lens. Phys Rev B 2011;84(2):024305.
[12] Gorshkov VN, et al. Sonic metamaterials: reflection on the role of topology on dispersion surface morphology. Mater Des 2017;132:44–56.
[13] Gorshkov VN, et al. Multi-resonator metamaterials as multi-band metastructures. Mater Des 2021:109522.
[14] Vo NH, et al. A reinvestigation of the spring-mass model for metamaterial bandgap prediction. Int J Mech Sci 2022;221:107219.
[15] Cai C, et al. The phononic band gaps of Bragg scattering and locally resonant pentamode metamaterials. J Phys D Appl Phys 2017;50:415105.
[16] Lee T, Iizuka H. Bragg scattering based acoustic topological transition controlled by local resonance. Phys Rev B 2019;99(6):064305.
[17] Xiao Y, et al. Theoretical and experimental study of locally resonant and bragg band gaps in flexural beams carrying periodic arrays of beam-like resonators. J Vib Acoust 2013;135(4):041006.
[18] Krushynska AO, et al. Coupling local resonance with Bragg band gaps in single-phase mechanical metamaterials. Extrem Mech Lett 2017;12:30–6.
[19] Cenedese M, Belloni E, Braghin F. Interaction of Bragg scattering bandgaps and local resonators in mono-coupled periodic structures. J Appl Phys 2021;129:124501.
[20] Lin S, et al. Bandgap characteristics and wave attenuation of metamaterials based on negative-stiffness dynamic vibration absorbers. J Sound Vib 2021;502:116088.
[21] Meng H, et al. 3D rainbow phononic crystals for extended vibration attenuation bands. Sci Rep 2020;10:18989.
[22] Oh JH, et al. Zero-frequency Bragg gap by spin-harnessed metamaterial. New J Phys 2018;20:083035.
[23] Vo NH, et al. Model for analytical investigation on meta-lattice truss for low-frequency spatial wave manipulation. Wave Motion 2021;103:102735.
[24] Vo NH, et al. Stress wave mitigation properties of dual-meta panels against blast loads. Int J Impact Eng 2021;154:103877.
[25] Vo NH, et al. Blast resistant enhancement of meta-panels using multiple types of resonators. Int J Mech Sci 2022;215:106965.
[26] Hu G, et al. Acoustic metamaterials with coupled local resonators for broadband vibration suppression. AIP Adv 2017;7:025211.

[27] Huang LZ, et al. Analysis of underwater decoupling properties of a locally resonant acoustic metamaterial coating. Chin Phys B 2016;25(2):024302.
[28] Zhang YY, et al. Low-frequency band gaps within a local resonance structures. Mod Phys Lett B 2020;34(1):2150014.
[29] Cao TNT, et al. A moving element method for the dynamic analysis of composite plate resting on a pasternak foundation subjected to a moving load. Int J Comput Methods 2018;16(8):1850124.
[30] Sheng P, Zhang XX, Liu Z, Chan CT. Locally resonant sonic materials. Phys B 2003;338(1–4):201–5.
[31] Wang P, et al. Harnessing buckling to design tunable locally resonant acoustic metamaterials. Phys Rev Lett 2014;113(1):014301.
[32] Palermo A, Vitali M, Marzani A. Metabarriers with multi-mass locally resonating units for broad band Rayleigh waves attenuation. Soil Dyn Earthq Eng 2018;113:265–77.
[33] Hu G, et al. Metamaterial with local resonators coupled by negative stiffness springs for enhanced vibration suppression. J Appl Mech 2019;86(8):081009.
[34] Yang M, Sheng P. Sound absorption structures: from porous media to acoustic metamaterials. Annu Rev Mater Res 2017;47:83–114.
[35] Finocchio G, et al. Seismic metamaterials based on isochronous mechanical oscillators. Appl Phys Lett 2014;104:191903.
[36] Chen YY, et al. Dissipative elastic metamaterials for broadband wave mitigation at subwavelength scale. Compos Struct 2016;136:358–71.
[37] Xu X, et al. Tailoring vibration suppression bands with hierarchical metamaterials containing local resonators. J Sound Vib 2019;442:237–48.
[38] Reichl KK, Inman DJ. Lumped mass model of a 1D metastructure for vibration suppression with no additional mass. J Sound Vib 2017;403:75–89.
[39] Liu Y, et al. Vibration attenuation of finite-size metaconcrete: Mechanism, prediction and verification. Compos Part A 2021;143:106294.
[40] Huang J, Shi Z. Attenuation zones of periodic pile barriers and its application in vibration reduction for plane waves. J Sound Vib 2013;332(19):4423–39.
[41] Zhu R, et al. A chiral elastic metamaterial beam for broadband vibration suppression. J Sound Vib 2014;333(10):2759–73.
[42] Hu G, et al. Metastructure With Piezoelectric Element for Simultaneous Vibration Suppression and Energy Harvesting. J Vib Acoust 2016;139(1):011012.
[43] Vo NH, et al. Impact load mitigation of meta-panels with Single Local Resonator. Eng Struct 2021;265:114528.
[44] Yan Y, et al. Seismic isolation of two dimensional periodic foundations. J Appl Phys 2014;116:044908.
[45] Yan Y, et al. Three dimensional periodic foundations for base seismic isolation. Smart Mater Struct 2015;24:075006.
[46] Miniaci M, et al. Large scale mechanical metamaterials as seismic shields. New J Phys 2016;18:083041.
[47] Shi Z, Cheng Z, Xiang H. Seismic isolation foundations with effective attenuation zones. Soil Dyn Earthq Eng 2014;57:143–51.
[48] Climente A, Torrent D, Sanchez-Dehesa J. Omnidirectional broadband insulating device for flexural waves in thin plates. J Appl Phys 2013;114(21):214903.
[49] Farhat M, et al. Broadband cylindrical acoustic cloak for linear surface waves in a fluid. Phys Rev Lett 2008;101(13):134501.
[50] Liu R, et al. Broadband ground-plane cloak. Science 2009;323(5912):366–9.
[51] Xia B, et al. Temperature-controlled tunable acoustic metamaterial with active band gap and negative bulk modulus. Appl Acoust 2016;112:1–9.
[52] Maldovan M. Phonon wave interference and thermal bandgap materials. Nat Mater 2015;14(7):667–74.
[53] Bacigalupo A, et al. Computational design of innovative mechanical metafilters via adaptive surrogate-based optimization. Comput Methods Appl Mech Eng 2021;375:113623.
[54] Bacigalupo A, et al. Machine-learning techniques for the optimal design of acoustic metamaterials. J Optim Theory Appl 2020;187:630–53.
[55] Fallah AS, et al. Phononic dispersion in anisotropic pseudo-fractal hyper-lattices. Mater Des 2019;164:107560.
[56] Huang GL, Sun CT. Band gaps in a multiresonator acoustic metamaterial. J Vib Acoust 2010;132(3):031003.
[57] Krushynska AO, et al. Spider web-structured labyrinthine acoustic metamaterials for low-frequency sound control. New J Phys 2017;19(10):105001.
[58] Frenzel T, et al. Three-dimensional labyrinthine acoustic metamaterials. Appl Phys Lett 2013;103(6):061907.
[59] Liu C, Xia B, Yu D. The spiral-labyrinthine acoustic metamaterial by coiling up space. Phys Lett A 2017;381(36):3112–8.
[60] Bacigalupo A, Gambarotta L. Simplified modelling of chiral lattice materials with local resonators. Int J Solids Struct 2016;83:126–41.
[61] Jin SG, Korkolis YP, Li YN. Shear resistance of an auxetic chiral mechanical metamaterial. Int J Solids Struct 2019;174:28–37.
[62] Man XF, et al. Hilbert fractal acoustic metamaterials with negative mass density and bulk modulus on subwavelength scale. Mater Des 2019;180:107911.
[63] Wang K, Liu Y, Liang T. Band structures in Sierpinski triangle fractal porous phononic crystals. Phys B 2016;498:33–42.
[64] Cassier M, DeGiovanni T, Guenneau S, Guevara Vasquez F. Active thermal cloaking and mimicking. Proc R Soc A 2021;477(2249):20200941.
[65] Maldovan M. Sound and heat revolutions in phononics. Nature 2013;503(7475):209–17.
[66] Popa BI, Zigoneanu L, Cummer SA. Tunable active acoustic metamaterials. Phys Rev B 2013;88(2):024303.
[67] Cummer SA, Rahm M, Schurig D. Material parameters and vector scaling in transformation acoustics. New J Phys 2008;10(11):115025.
[68] Popa BI, et al. Active acoustic metamaterials reconfigurable in real time. Phys Rev B 2015;91(22):220303.
[69] Ginder JM, et al. Magnetorheological elastomers: properties and applicationsWuttig M, editor. . Smart structures and materials: smart materials technologies, 3675. Proc. SPIE; 1999. p. 131–8.
[70] Stepanov GV, et al. Effect of a homogeneous magnetic field on the viscoelastic behavior of magnetic elastomers. Polymer 2007;48(2):488–95.
[71] Boczkowska A, Awietjan S, Boczkowska A. Microstructure and properties of magnetorheological elastomers. Advances in elastomers – technology, properties and applications. IntechOpen; 2012. p. 147–80.
[72] Li WH, Zhang XZ, Du H, Visakh PM, et al. Magnetorheological elastomers and their applications. Advances in elastomers I: blends and interpenetrating. Berlin, Heidelberg: Springer; 2013. p. 357–74. 11.
[73] Lokander M, Stenberg B. Performance of isotropic magnetorheological rubber materials. Polym Test 2003;22(3):245–51.
[74] Zając P, et al. Isotropic magnetorheological elastomers with thermoplastic matrices: structure, damping properties and testing. Smart Mater Struct 2010;19(4):045014.
[75] Zhu JT, Xu ZD, Guo YQ. Experimental and modeling study on magnetorheological elastomers with different matrices. J Mater Civ Eng 2013;25(11):1762–71.
[76] Liu T, Xu Y, Dong X. Magnetorheological elastomers: materials and applications. Smart and functional soft materials. IntechOpen; 2019. p. 147–80.
[77] Kukla M, et al. Magnetorheological elastomer stress relaxation behaviour during compression: experiment and modelling. Materials 2020;13(21):4795.
[78] Samal S, et al. Magneto-rheological elastomer composites. a review. Appl Sci 2020;10(14):4899.
[79] Li T, et al. Investigate the effect of the magnetic field on the mechanical properties of silicone rubber-based anisotropic magnetorheological elastomer during curing process. J Renew Mater 2020;8(11):1411–27.
[80] Dargahi A, Sedaghati R, Rakheja S. On the properties of magnetorheological elastomers in shear mode: design, fabrication and characterization. Compos Part B Eng 2019;159:269–83.
[81] Deng HX, Gong XL. Application of magnetorheological elastomer to vibration absorber. Commun Nonlinear Sci Numer Simul 2008;13(9):1938–47.
[82] Kim HK, Kim HS, Kim YK. Stiffness control of magnetorheological gels for adaptive tunable vibration absorber. Smart Mater Struct 2017;26(2):015016.
[83] Liao GJ, et al. Development of a real-time tunable stiffness and damping vibration isolator based on magnetorheological elastomer. J Intell Mater Syst Struct 2012;23(1):25–33.
[84] Bastola AK, Li L. A new type of vibration isolator based on magnetorheological elastomer. Mater Des 2018;157:431–6.
[85] Liu A, et al. A real-time controllable electromagnetic vibration isolator based on magnetorheological elastomer with quasi-zero stiffness characteristic. Smart Mater Struct 2019;28(8):045014.
[86] Qi S, et al. Magnetorheological elastomers enabled high-sensitive self-powered tribo-sensor for magnetic field detection. Nanoscale 2018;10:4745–52.
[87] Hu T, et al. Stretchable and magneto-sensitive strain sensor based on silver nanowire-polyurethane sponge enhanced magnetorheological elastomer. Mater Des 2018;156:528–37.
[88] Bose H, Rabindranath R, Ehrlich J. Soft magnetorheological elastomers as new actuators for valves. J Intell Mater Syst Struct 2012;23(9):989–94.
[89] Ladipo IL, Fadly JD, Faris WF. Characterization of magnetorheological elastomer (MRE) engine mounts. Mater Today Proc 2016;3(2):411–8.
[90] Li Y, et al. A highly adjustable magnetorheological elastomer base isolator for applications of real-time adaptive control. Smart Mater Struct 2013;22(9):095020.
[91] Hu W, et al. Small-scale soft-bodied robot with multimodal locomotion. Nature 2018;554:81–5.
[92] Kim Y, et al. Ferromagnetic soft continuum robots. Sci Robot 2019;4(33):eaax7329.
[93] Mitsumata T, Ohori S. Magnetic polyurethane elastomers with wide range modulation of elasticity. Polym Chem 2011;2(5):1063–7.
[94] Mitsumata T, et al. Magnetism and viscoelasticity of magnetic elastomers with wide range modulation of dynamic modulus. Soft Matter 2013;9(3):904–12.
[95] Nagashima K, Mitsumata T. Magnetorheological effect for bimodal magnetic elastomers. Int Polym Sci Technol 2017;44(6):45–50.
[96] Borin D, et al. Magnetorheological effect of magnetoactive elastomer with a permalloy filler. Polymers 2020;12(10):2371.
[97] Linke JuliaM, Borin DY, Odenbach S. First-order reversal curve analysis of magnetoactive elastomers. RSC Adv 2016;6(102):100407–16.
[98] Böse H, Röder R. Magnetorheological elastomers with high variability of their mechanical properties. J Phys Conf Ser 2009;149:012090.
[99] Kashima S, Miyasaka F, Hirata K. Novel soft actuator using magnetorheological elastomer. IEEE Trans Magn 2012;48(4):1649–52.
[100] Du H, Li W, Zhang N. Semi-active variable stiffness vibration control of vehicle seat suspension using an MR elastomer isolator. Smart Mater Struct 2011;20(10):105003.